Available online at www.sciencedirect.com
SCIENCE DIRECT®
Engineering Fracture Mechanics 72 (2005) 1954–1979
Engineering Fracture Mechanics
www.elsevier.com/locate/engfracmech

Crack propagation due to brittle and ductile failures in microporous thermoelastoviscoplastic functionally graded materials

R.C. Batra *, B.M. Love

Engineering Science and Mechanics, MC 0219, Virginia Polytechnic Institute and State University, Blacksburg, VA 24061, United States

Received 27 July 2004; received in revised form 21 September 2004; accepted 5 November 2004
Available online 24 March 2005

R.C. Batra dedicates this work to Professor YiLong Bai on his 65th birthday

Abstract

Plane strain transient finite thermomechanical deformations of heat-conducting functionally gradient materials comprised of tungsten and nickel–iron matrix are analyzed to delineate brittle/ductile failures by the nodal release technique. Each material is modeled as strain-hardening, strain-rate-hardening and thermally-softening. Effective properties are derived by the rule of mixtures. At nominal strain-rate of 2000 s^{-1} brittle crack speed approaches Rayleigh's wave speed in the tungsten-plate, the nickel–iron-plate shatters at strain-rates above 1130 s^{-1}, and the composite plate does not shatter. The maximum speed of a ductile crack in tungsten and nickel–iron is about 1.5 km/s, and that in the composite is about 0.14 km/s.

Keywords: Node release technique; Crack speed; Finite element method; Shear bands; Transient finite plastic deformations

1. Introduction

Modeling crack propagation during the solution of a transient problem by the finite element method (FEM) is very challenging since the crack initiation point and its path are to be determined as a part of the solution of the problem. Three strategies often used to analyze fracture are: (i) introducing cohesive elements along inter-element boundaries that are weak in shear and tension but very strong in compression;

* Corresponding author. Tel.: +1 540 231 6051; fax: +1 540 231 4574.
E-mail addresses: rbatra@vt.edu (R.C. Batra), brlove@vt.edu (B.M. Love).

0013-7944/$ - see front matter © 2005 Elsevier Ltd. All rights reserved.
doi:10.1016/j.engfracmech.2004.11.010

(ii) representing a crack as two traction-free surfaces by placing two coincident but unconnected nodes at the crack initiation point and relieving tractions on the newly created crack surfaces; and (iii) reducing elastic constants and stresses developed in the failed region to zero and virtually eliminating these elements from the analysis of the problem; it is usually referred to as the element deletion method. Each of these techniques has its advantages and disadvantages. Technique (i) has often been used to simulate brittle failure wherein strains induced are small and very little plastic deformations occur. When used to study ductile failure, it does not allow for the incorporation of frictional forces between two sliding surfaces formed during the failure process. Whereas technique (iii) can accommodate large plastic deformations, it also does not permit the consideration of sliding between adjacent surfaces surrounding the failed region. Wang and Nakamura [1] have discussed four techniques for simulating material failure; however technique (ii) is not one of them. They adopted technique (i) to analyze failure in TiB/Ti functionally graded (FG) ceramic/metal plate in which brittle failure ensues at rather small strains. They modeled the plate material as elastic–plastic and considered inertia forces. An accurate modeling of the crack path and hence its speed of propagation requires a very fine FE mesh.

Functionally graded materials (FGMs) are a class of materials in which material properties vary gradually and continuously so as to optimize their performance under prescribed loads. For example, Hasselman and Youngblood [2] have shown that the thermal stress resistance of a structural ceramic can be enhanced by properly grading its thermal conductivity. Qian and Batra [3] found the in-plane spatial variation in the volume fractions of constituents to optimize the first or the second natural frequency of a FG plate with one edge clamped. Batra and Jin [4] determined the continuous variation in the fiber orientation angle for an anisotropic graphite/epoxy plate in order to optimize its first few natural frequencies.

Most studies (e.g., see [5–12]) on fracture of FGMs have considered their static linear elastic deformations. Following an earlier study of a propagating crack by Atkinson and List [12], there have been at least three studies [13–15] on analyzing propagating cracks in FGMs. Recently, Lee [15] developed displacement and stress fields ahead of a crack propagating at a uniform velocity in a FGM with shear modulus either varying linearly ahead of the crack-tip and Poisson's ratio and mass density kept constant or the shear modulus and mass density varying exponentially but Poisson's ratio kept constant.

Works that have analyzed the elastic–plastic fracture of FGMs include that of Jin and Noda [6] who showed that the HRR singularity exists near a stationary crack tip in a power-law hardening material provided the yield stress and the hardening exponent are continuous and piecewise continuously differentiable functions of the effective plastic strain. Tvergaard [16] modeled the interface between two power-law materials with a graded elastic–plastic layer and investigated crack growth in the FG layer using a cohesive zone model with constant peak cohesive traction and cohesive energy density. Jin and Dodds [17] have analyzed the crack growth resistance behavior of a ceramic/metal FGM with the background material modeled by the J_2 flow theory and undergoing three-dimensional quasistatic plastic deformations. They simulated crack propagation with a cohesive zone model having six material dependent parameters. Small plastic deformations are concentrated near the crack-tip and the crack growth resistance, calculated by the J-integral, was found to increase significantly with the crack extension due to gradation in material properties. Wang and Nakamura [1] used the cohesive zone model to analyze transient infinitesimal elastic–plastic deformations of a dynamically loaded FG plate. They simulated brittle fracture and found that the energy of separation constituted a small part of the total fracture energy. The former was computed from the cohesive law and the latter equaled the sum of the separation energy and the energy dissipated due to plastic deformations. Thus, a large plastic dissipation translates to higher crack growth resistance. However, no thermal effects, such as heat conduction and material softening due to heating, were considered.

Here we analyze transient plane strain coupled thermomechanical finite deformations of a microporous thermoelastoviscoplastic FG body comprised of tungsten (W) and nickel–iron (NiFe). We assume that a crack due to brittle failure initiates at a point when the maximum principal tensile stress there reaches three times the quasistatic yield stress, and a crack due to ductile failure ensues when the effective plastic strain

equals 1.5. The body is either loaded axially in tension to induce brittle failure or in shear to simulate the ductile failure. Thus only one mode of failure can initiate in the body. As soon as a fracture criterion is met at a node N, two coincident but unconnected nodes are located there and joined to the node N^*. The node N^* is selected so that the gradient of the failure variable is least along the line NN^*. If a gap develops between the newly created crack surfaces, then they are taken to be traction free and thermally insulated; otherwise they are taken to be smooth and thermally insulated. In the former case all components of traction, and in the latter case only tangential tractions are gradually reduced to zero. However, in each case the normal component of heat flux is set equal to zero instantaneously. Thus elastic unloading waves emanate from the crack surfaces and propagate into the body. By locating the crack tip at different times, we ascertain its speed.

The paper is organized as follows. Section 2 summarizes the governing equations, initial and boundary conditions, non-dimensionalization of equations, homogeneziation of material properties, semi-discrete formulation of the problem, failure criteria for brittle and ductile fractures, and the technique adopted to simulate the crack propagation. In Section 3, we compare numerical solution of wave propagation in a linear elastic FG bar with the analytical solution of the problem, and present results for brittle and ductile failure propagation in W and NiFe plates as well as NiFe2W and W2NiFe FG plates; material properties vary continuously from those of NiFe to those of W in a NiFe2W plate. We also remark on the effectiveness of the present approach. Section 4 summarizes conclusions drawn from this study.

2. Formulation of the problem

2.1. Governing equations

We use rectangular Cartesian coordinates and the referential description of motion to describe finite plane strain transient coupled thermomechanical deformations of an isotropic and microporous thermoelastoviscoplastic FG body. Deformations of each constituent and the composite body are governed by following equations expressing, respectively, the balance of mass, the balance of linear momentum, the balance of moment of momentum, and the balance of internal energy:

$$\rho(1-f)J = \rho_0(1-f_0), \tag{1}$$

$$\rho_0(1-f_0)\dot{v}_i = T_{i\alpha,\alpha}, \quad i,j = 1,2, \ \ \alpha = 1,2, \tag{2}$$

$$T_{i\alpha}F_{j\alpha} = T_{j\alpha}F_{i\alpha}, \tag{3}$$

$$\rho_0(1-f_0)\dot{e} = -Q_{\alpha,\alpha} + T_{i\alpha}\dot{F}_{i\alpha}. \tag{4}$$

Here ρ is the present mass density, f the porosity (i.e., the volume fraction of voids), $J = \det \mathbf{F}$, $F_{i\alpha} = x_{i,\alpha} = \partial x_i/\partial X_\alpha$ the deformation gradient, $\mathbf{x}$ the present position at time t of a material particle located at the place $\mathbf{X}$ in the reference configuration, $\mathbf{T}$ the first Piola–Kirchhoff stress tensor, e the specific internal energy, $\mathbf{Q}$ the present heat flux measured per unit reference area, $\mathbf{v}$ the velocity of a material particle, a superimposed dot indicates the material time derivative, and a repeated index implies summation over the range of the index. Greek indices refer to coordinates in the reference configuration, and Latin indices to coordinates in the present configuration.

We assume that the strain-rate tensor $\mathbf{D}$ defined by $D_{ij} = (v_{i,j} + v_{j,i})/2$, $v_{i,j} = \partial v_i/\partial x_j$, has the additive decomposition into an elastic part $\mathbf{D}^e$, a plastic part $\mathbf{D}^p$ and a thermal part $\hat{\alpha}\dot{\theta}\mathbf{1}$, viz., $\mathbf{D} = \mathbf{D}^e + \mathbf{D}^p + \hat{\alpha}\dot{\theta}\mathbf{1}$. Here $\hat{\alpha}$ is the coefficient of thermal expansion, θ the temperature rise and $\mathbf{1}$ the identity tensor. Eqs. (1)–(4) are supplemented with the following constitutive relations:

$$\dot{\sigma}_{ij} + \sigma_{ik}W_{kj} + \sigma_{jk}W_{ki} = \frac{E(1-f)}{1+\nu}D^e_{ij} + \frac{E(1-f)\nu}{(1+\nu)(1-2\nu)}D^e_{kk}\delta_{ij}, \tag{5}$$

$$\dot{e} = c\tau\ddot{\theta} + c\dot{\theta} + \frac{1}{\rho(1-f)}\sigma_{ij}D^{\mathrm{e}}_{ij}, \qquad T_{i\alpha} = J\sigma_{ij}(F^{-1})_{\alpha j}, \tag{6}$$

$$q_i = -\kappa\left(1 - \frac{3}{2}f\right)\theta_{,i}, \qquad Q_\alpha = Jq_i(F^{-1})_{\alpha i}, \tag{7}$$

$$\phi \equiv \frac{\sigma_{\mathrm{e}}^2}{\sigma_{\mathrm{y}}^2} - 1 + 2f^*\beta_1\cosh\left(\frac{3\beta_2\bar{p}}{2\sigma_{\mathrm{y}}}\right) - \beta_1^2(f^*)^2 = 0, \qquad \sigma_{\mathrm{e}}^2 = \frac{3}{2}\sigma'_{ij}\sigma'_{ij}, \quad i,j = 1,2,3, \tag{8}$$

$$D^{\mathrm{p}}_{ij} = \dot{\lambda}\frac{\partial\phi}{\partial\sigma_{ij}} = \dot{\lambda}\left[\frac{3\sigma'_{ij}}{\sigma_{\mathrm{y}}^2} - \frac{f^*\beta_1\beta_2}{\sigma_{\mathrm{y}}}\sinh\left(\frac{3\beta_2\bar{p}}{2\sigma_{\mathrm{y}}}\right)\delta_{ij}\right], \qquad \sigma'_{ij} = \sigma_{ij} + p\delta_{ij}, \tag{9}$$

$$p = -(\sigma_{11} + \sigma_{22} + \sigma_{33})/3, \quad \bar{p} = pH(-p-0), \tag{10}$$

$$\dot{\lambda} = \begin{cases} \dfrac{(1-f)\sigma_{\mathrm{y}}\dot{\varepsilon}^{\mathrm{p}}_{\mathrm{e}}}{\sigma_{ij}\dfrac{\partial\phi}{\partial\sigma_{ij}}}, & \text{if } \phi = 0 \text{ and } \dot{\phi} \geqslant 0, \\ 0 & \text{when either } \phi < 0 \text{ or } \phi = 0 \text{ and } \dot{\phi} < 0, \end{cases} \tag{11}$$

$$\dot{f} = (1-f)D^{\mathrm{p}}_{ii} + \frac{f_2\dot{\varepsilon}^{\mathrm{p}}_{\mathrm{e}}}{s_2\sqrt{2\pi}}\exp\left\{-\frac{1}{2}\left(\frac{\varepsilon^{\mathrm{p}}_{\mathrm{e}} - \varepsilon_n}{s_2}\right)^2\right\}H(-p-0), \tag{12}$$

$$f^* = \begin{cases} f, & f \leqslant f_{\mathrm{c}}, \\ f_{\mathrm{c}} + \dfrac{f_{\mathrm{u}} - f_{\mathrm{c}}}{f_{\mathrm{f}} - f_{\mathrm{c}}}(f - f_{\mathrm{c}}), & f > f_{\mathrm{c}}, \end{cases} \tag{13}$$

$$\sigma_{\mathrm{y}} = (A + B(\varepsilon^{\mathrm{p}}_{\mathrm{e}})^n)\left(1 + \widetilde{C}\ln\left(\frac{\dot{\varepsilon}^{\mathrm{p}}_{\mathrm{e}}}{\dot{\varepsilon}^{\mathrm{p}}_0}\right)\right)\left(1 - \left(\frac{\theta - \theta_{\mathrm{r}}}{\theta_{\mathrm{m}} - \theta_{\mathrm{r}}}\right)^m\right). \tag{14}$$

The left-hand side of Eq. (5) equals the Jaumann derivative of the Cauchy stress tensor $\boldsymbol{\sigma}$, $W_{ij} = (v_{i,j} - v_{j,i})/2$ is the spin tensor, E Young's modulus, ν Poisson's ratio, c the specific heat, τ the thermal relaxation time, κ the thermal conductivity of the solid material, and θ the present temperature of a material particle. $\phi = 0$ describes the yield surface proposed by Gurson [18] for a porous material, p is the hydrostatic pressure, and f^* the modified value of porosity given by (13). Gurson's yield surface is based on quasistatic analysis with the matrix material modeled as rigid perfectly plastic and obeying von Mises yield criterion. Constants β_1 and β_2, introduced by Tvergaard [19], provide a better fit of results computed from a FE analysis of the formation of ASBs in a plate having an array of large cylindrical voids with test observations, and $\dot{\lambda}$ is the factor of proportionality defined by (11); $\dot{\lambda} > 0$ only when the material point is deforming plastically. σ_{y} is the current yield stress of the material whose dependence upon the effective plastic strain $\varepsilon^{\mathrm{p}}_{\mathrm{e}}$, the effective plastic strain rate $\dot{\varepsilon}^{\mathrm{p}}_{\mathrm{e}}$ and the temperature θ is described by the Johnson–Cook [20] relation (14) in which A, B, n, $\widetilde{C}$, $\dot{\varepsilon}^{\mathrm{p}}_0$, and m are material parameters, θ_{r} the room temperature and θ_{m} the melting temperature of the material. Parameters B and n characterize the strain hardening of the material, C and $\dot{\varepsilon}^{\mathrm{p}}_0$ the strain-rate hardening and the last factor on the right-hand side of (14) its thermal softening. Eq. (12) gives the evolution of porosity; the first term on its right-hand side is derived by assuming that the matrix is incompressible and the elastic dilatation is negligible as compared to the plastic dilatation, and the second term is the strain based nucleation of voids introduced by Chu and Needleman [21]. f_2, s_2 and ε_n are material parameters; the rate of nucleation of voids is highest when $\varepsilon^{\mathrm{p}}_{\mathrm{e}}$ equals ε_n and decays exponentially with

the difference between ε_e^p and ε_n. H is the Heaviside step function. Thus the second term contributes to the evolution of porosity at a point only when the hydrostatic pressure there is tensile. To account for the coalescence of neighboring voids, Tvergaard and Needleman [22] enhanced the porosity, as given by Eq. (13), after it reaches its critical value f_c. In Eq. (13), f_f is the porosity at ductile fracture, and $f_u = 1/\beta_1$ is the porosity when the yield surface has shrunk to a point. Eqs. (8) and (14) imply that the radius of the von Mises yield surface increases due to strain- and strain-rate hardening of the material but decreases due to the softening induced by the temperature rise and the increase in porosity. The degradation of material properties due to the damage, taken here synonymous with the porosity, is indicated by Eqs. (5)–(8). The affine variation with the porosity of Young's modulus, the bulk modulus, the stress-temperature coefficient, and the heat capacity implies that the rule of mixture has been employed to find their effective values; the expression for the thermal conductivity in Eq. $(7)_1$ is due to Budiansky [23]. The interaction, if any, among neighboring voids has been tacitly ignored. Jiang and Batra [24], among others, have considered this interaction. The shrinkage of the yield surface due to an increase in porosity described by Eq. (8) can be seen by plotting the yield surface for two different values of f while keeping other variables fixed.

For a FG body, all thermophysical parameters may vary with $\mathbf{X}$.

Substitution from Eqs. $(6)_1$ and (7) into (4) gives the following hyperbolic heat equation:

$$\rho_0(1-f_0)c(\tau\ddot{\theta}+\dot{\theta}) = \left(\kappa\left(1-\frac{3}{2}f\right)\theta_{,\alpha}\right)_{,\alpha} + J\sigma_{ij}D_{ij}^p. \tag{15}$$

The term $J\sigma_{ij}D_{ij}^p$ equals the heating due to plastic working per unit volume in the reference configuration; thus the Taylor–Quinney parameter has been taken as 1. Except for a delay in the time of initiation of the ductile failure other results remain unaffected by a lower value of the Taylor–Quinney factor. The form (15) of the hyperbolic heat equation is due to Cattaneo [25] and Vernotte [26]. The thermal relaxation time τ in it represents the time required to establish a steady state of heat conduction in an element suddenly exposed to heat flux. For a typical steel, $\tau = 1\times10^{-12}$ s, and $\tau \simeq 25\times10^{-12}$ s for copper. Batra and coworkers [27,28] found that the finiteness of the thermal wave speed affects the time of initiation of an adiabatic shear band in a typical steel and the spacing between adjacent shear bands only when $\tau \geqslant 10^{-6}$ s. Batra [29] considered higher-order spatial and temporal gradients of temperature and derived a heat equation that admits finite speeds of thermal waves. However, in such a material either a thermal wave propagates with a finite speed or the linearized problem has a unique solution. Ideally, one will like to have both.

We note that Batra and coworkers [30,31,28,32] have analyzed different aspects of shear banding with four different thermoviscoplastic relations, namely, the Johnson–Cook [20], the Litonski–Batra (e.g. see [33]), the Bodner–Partom [34] and a power law. These relations were calibrated to give nearly the same effective stress vs. the effective strain curve during homogeneous deformations of the body. However, during inhomogeneous deformations, each one of the relations gave qualitatively similar but quantitatively different results. The decision to use the Johnson–Cook relation here is based on the availability of values of thermomechanical parameters for different materials.

2.2. Initial and boundary conditions

The body is initially at rest, stress free, at a uniform temperature, and has zero rate of change of temperature and zero initial porosity. Thus

$$\begin{aligned} &\mathbf{x}(\mathbf{X},0)=\mathbf{X}, \quad \mathbf{v}(\mathbf{X},0)=\mathbf{0}, \quad \theta(\mathbf{X},0)=\theta_0, \quad \dot{\theta}(\mathbf{X},0)=0, \quad \rho(\mathbf{X},0)=\rho_0, \quad (\mathbf{X}),\\ &\boldsymbol{\sigma}(\mathbf{X},0)=\mathbf{0}, \quad \varepsilon_e^p(\mathbf{X},0)=0, \quad f(\mathbf{X},0)=f_0(\mathbf{X}), \quad \mathbf{X}\in\Omega. \end{aligned} \tag{16}$$

Here Ω is the region occupied by the body in the reference configuration.

We assume that the body is prismatic having a uniform cross-section (i.e. volume fractions of constituents are independent of the axial coordinate), and boundary conditions are independent of the axial coordinate. We thus assume that a plane strain state of deformation prevails in the body. Furthermore, for the body deformed in simple tension, the cross-section is a square of side $2H$, and thermomechanical deformations are assumed to be symmetric about the two centroidal axes. Thus the compositional profile has been tacitly assumed to be symmetric about the two centroidal axes. When analyzing crack propagation due to brittle failure, tensile deformations of half of the cross-section, shown in Fig. 1a, are analyzed. Symmetry about the horizontal centroidal axis is not exploited because of the way our crack propagation algorithm works. Boundary conditions $((17)_{4-6})$, listed below, arising from the symmetry of deformations are imposed at points on the centroidal axis $X_1 = 0$. The other vertical surface $X_1 = H$ is taken to be traction free and thermally insulated; see Eq. $((17)_{1-3})$. Normal velocity, null tangential tractions and zero heat flux are prescribed on the top horizontal surface $X_2 = H$; these are given by Eq. $(17)_{7-9}$. The prescribed normal velocity, given by Eq. $(17)_9$, increases linearly with time to its steady state value v_0 in 1 μs and is then held fixed:

$$\begin{aligned} &T_{21} = T_{11} = 0, \quad Q_1 = 0 \qquad \text{on } X_1 = H, \\ &T_{21} = 0, \quad v_1 = 0, \quad Q_1 = 0 \qquad \text{on } X_1 = 0, \\ &T_{12} = 0, \quad Q_2 = 0, \quad v_2 = \begin{cases} \pm v_0 t, & 0 \leqslant t \leqslant 1\ \mu\text{s}, \\ \pm v_0, & t \geqslant 1\ \mu\text{s}, \end{cases} \qquad \text{on } X_2 = \pm H. \end{aligned} \tag{17}$$

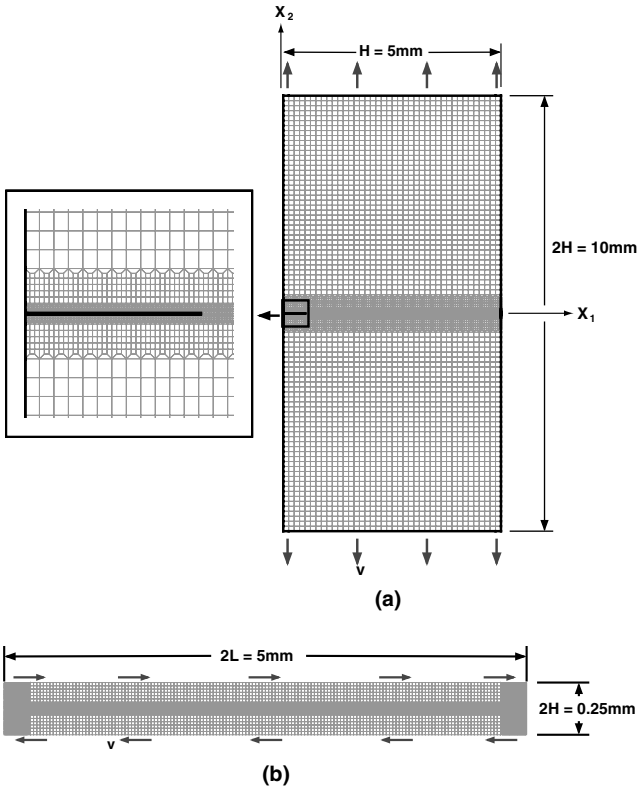

Fig. 1. (a) FE mesh for plane strain tensile deformations of a precracked plate, the inset shows details of the mesh around the cracked region; (b) FE mesh for plane strain shear deformations of a plate.

When studying plane strain shear deformations for analyzing ductile failure, the cross-section is of infinite length along the X_1-axis and of height $2H$. However, deformations of the region $[-L, L]\times[-H, H]$ are analyzed, and displacements and temperature of points on surfaces $X_1 = \pm L$ are constrained to be same. The top and bottom surfaces are taken to be thermally insulated and restrained from moving vertically. Equal and opposite tangential velocity v_1 that increases linearly with time from zero to its steady value v_0 in 1 μs is applied. Thus on $x_2 = X_2 = \pm H$, we have

$$Q_2 = 0, \quad v_2 = 0, \quad v_1 = \begin{cases} \pm v_0 t, & 0 \leqslant t \leqslant 1\ \mu\text{s}, \\ v_0, & t > 1\ \mu\text{s}. \end{cases} \tag{18}$$

For $t > 1$ μs, the average shear strain rate is v_0/H. Note that only the top and the bottom surfaces are restrained from moving vertically and other material particles are free to move in the x_1x_2-plane.

2.3. Non-dimensionalization of variables

Let ρ_R, $\dot{\varepsilon}_R$, H, σ_0 and θ_R be the reference mass density, the reference strain rate, the reference length, the reference stress and the reference temperature used to non-dimensionalize quantities. Then in terms of non-dimensional variables indicated by the same symbols as before, Eqs. (2) and (15) become

$$\alpha_I(1 - f_0)\dot{v}_i = T_{i\alpha,\alpha}, \quad i = 1, 2, \ \ \alpha = 1, 2, \tag{19}$$

$$\rho_0(1 - f_0)(\tau\ddot{\theta} + \dot{\theta}) = -\alpha_t\left(\left(1 - \frac{3}{2}f\right)\theta_{,\alpha}\right)_{,\alpha} + J\sigma_{ij}D^p_{ij}, \quad i, j = 1, 2, 3. \tag{20}$$

Here

$$\alpha_I = \frac{\rho_R\dot{\varepsilon}_R^2H^2}{\sigma_0}, \qquad \alpha_t = \frac{\kappa}{\rho_R cH^2\dot{\varepsilon}_R}, \qquad \theta_R = \frac{\sigma_0}{\rho_R c}; \tag{21}$$

α_I and α_t are non-dimensional measures of inertia and heat conduction effects respectively. For a given material, inertia effects are directly proportional to the square of the reference strain rate and the square of the reference length, and heat conduction effects are inversely proportional to the reference strain rate and the square of the reference length. A possible choice for $2H$ is the length of a side of the square cross-section for the plane strain problem, and the thickness of the block for the simple shearing problem, and that for $\dot{\varepsilon}_R$ is v_0/H.

2.4. Composition of a FG plate

Transient thermomechanical deformations of a FG plate comprised of tungsten (W) and nickel–iron (NiFe) are studied. Each constituent and the composite are modeled as isotropic, microporous, thermoelastoviscoplastic with deformations governed by Eqs. (19), (20) and (5)–(14). For the plane strain problem, the volume fractions of W in W2NiFe and NiFe2W plates are given by $(1 - |X_1|/H)$ and $|X_1|/H$ respectively. Here $2H$ is the plate width. Thus in a NiFe2W plate, the composition profile varies linearly from 0% W at $X_1 = 0$ to 100% W at $X_1 = H$.

2.5. Homogenization of material properties

We first analyzed transient deformations of a representative volume element (RVE) to evaluate effective properties of the composite as a function of the volume fraction of constituents. Values of material parameters characterizing elastic deformations so determined were found to match well with those given by the Mori–Tanaka [35] scheme. Values of material parameters characterizing the plastic deformation could not

be satisfactorily determined from deformations of the RVE differ from those given by the rule of mixtures by about 10% (see [53]). We thus use the rule of mixtures to evaluate values of all material parameters from those of the constituents and their volume fractions. According to this rule, the value P of a material parameter for a mixture comprised of two constituents with volume fractions V_1^{f} and V_2^{f} and values P_1 and P_2 of the material parameter is given by

$$P = V_1^{\mathrm{f}} P_1 + V_2^{\mathrm{f}} P_2 = (1 - V_2^{\mathrm{f}}) P_1 + V_2^{\mathrm{f}} P_2. \tag{22}$$

It gives exact values of the mass density and the heat capacity, and is simple to use. It ignores interactions among adjacent particulates, their shapes and sizes, and their distribution in the matrix. We note that no micromechanical models have been developed for evaluating all material parameters for a FGM comprised of thermoviscoplastic constituents.

Suquet [36] has given a closed-form expression for the yield stress of an isotropic homogenized body made of isotropic elastic perfectly plastic constituents. The estimate of the yield stress involves effective shear modulus of the composite. For a W/NiFe FG body, the difference in the effective yield stress computed from Suquet's expression and that obtained by the rule of mixtures is less than 10%.

2.6. Semi-discrete formulation of the problem

Eqs. (5), $(6)_2$ and (3) imply that the balance of moment of momentum (3) is identically satisfied. The present mass density can be computed from Eq. (1) if the deformation gradient and the current value of the porosity are known. Thus, the dependent variables to be solved for are $\mathbf{x}$, f and θ and the independent variables are $\mathbf{X}$ and t. Eqs. (19) and (20) are second-order coupled nonlinear hyperbolic partial differential equations for $\mathbf{x}$ and θ. These cannot be written explicitly in terms of $\mathbf{x}$ and θ since $\mathbf{T}$ is given by $(6)_2$ and $\dot{\boldsymbol{\sigma}}$ by (5) which involves $\mathbf{D}^{\mathrm{p}}$ and θ. We solve the problem numerically by the FEM.

We first introduce an auxiliary variable $\xi = \dot{\theta}$. Let $\psi_1, \psi_2, \ldots, \psi_n$ be the FE basis functions defined on Ω. We write

$$v_i = \sum_{A=1}^{\text{nodes}} \psi_A(\mathbf{x}) \widetilde{v}_{Ai}(t), \quad w_i = \sum_{A=1}^{\text{nodes}} \psi_A(\mathbf{X}) c_{Ai}, \quad \theta = \sum_{A=1}^{\text{nodes}} \psi_A(\mathbf{X}) \widetilde{\theta}_A, \quad \xi = \sum_{A=1}^{\text{nodes}} \psi_A(\mathbf{X}) \widetilde{\xi}_A, \qquad i = 1, 2. \tag{23}$$

Here $\tilde{\mathbf{v}}$ is the vector of velocities of nodes, $\tilde{\boldsymbol{\theta}}$ the vector of nodal temperatures, $\tilde{\boldsymbol{\xi}}$ the vector of rate of change of temperature at the nodes, and c's are constants. Following the usual procedure, e.g. see [37], we get

$$\mathbf{M}\dot{\tilde{\mathbf{v}}} = -\mathbf{F}^{\mathrm{int}}, \qquad \dot{\boldsymbol{\theta}} = \tilde{\boldsymbol{\xi}}, \qquad \tau \mathbf{H}\dot{\tilde{\boldsymbol{\xi}}} + \mathbf{H}\tilde{\boldsymbol{\xi}} = \mathbf{F}^{\theta} + \widetilde{\mathbf{Q}}, \tag{24}$$

where

$$\begin{aligned} M_{AB} &= \int_{\Omega} \alpha_1 (1 - f_0) \psi_A \psi_B \, \mathrm{d}\Omega, \qquad F_{Ai}^{\mathrm{int}} = \int_{\Omega} \psi_{A,\alpha} T_{i\alpha} \, \mathrm{d}\Omega, \\ H_{AB} &= \int_{\Omega} \rho_0 (1 - f_0) \psi_A \psi_B \, \mathrm{d}\Omega, \qquad F_A^{\theta} = \int_{\Omega} \alpha_{\mathrm{t}} \left(1 - \frac{3}{2} f\right) \theta_{,\alpha} \psi_{A,\alpha} \, \mathrm{d}\Omega, \\ Q_A &= \int_{\Omega} \psi_A J \, \mathrm{tr}(\boldsymbol{\sigma} \mathbf{D}^{\mathrm{p}}) \, \mathrm{d}\Omega. \end{aligned} \tag{25}$$

Note that the natural boundary condition of zero heat flux has been embedded in Eq. $(24)_3$.

We solve Eq. (14) for $\dot{\varepsilon}_{\mathrm{e}}^{\mathrm{p}}$ in terms of σ_{y}, $\varepsilon_{\mathrm{e}}^{\mathrm{p}}$ and θ and derive its weak form in the same way as before except that the divergence theorem is not used. Recall that $\dot{\varepsilon}_{\mathrm{e}}^{\mathrm{p}} > 0$ only when a material point is deforming plastically as signified by the satisfaction of Eq. $(8)_1$; otherwise $\dot{\varepsilon}_{\mathrm{e}}^{\mathrm{p}} = 0$. Weak forms of Eqs. (6), (14) and $\dot{\mathbf{x}} = \mathbf{v}(\mathbf{X}, t)$ are also derived. We thus get coupled nonlinear ordinary differential equations

$$\dot{\mathbf{d}} = \mathbf{F}, \tag{26}$$

where $\mathbf{d}$ is the vector of unknowns and $\mathbf{F}$ is the force vector that depends upon time t and $\mathbf{d}(t)$. The twelve unknowns at a node are $\{x_1, x_2, v_1, v_2, \sigma_{11}, \sigma_{22}, \sigma_{12}, \sigma_{33}, f, \theta, \xi, \varepsilon_e^p\}$, and the dimension of vector $\mathbf{d}$ equals 12 times the number of nodes.

2.7. Failure initiation criterion

2.7.1. Brittle failure

Ritchie et al. [38] proposed that the brittle failure initiates at a point when $\sigma_p/\sigma_0 = 3.0$ over a certain length that depends upon the microstructure of the material and usually equals a grain diameter. Here σ_p and σ_0 equal, respectively, the maximum principal tensile stress at a point and the yield stress in a quasi-static simple tension/compression test at the same point. For the Johnson–Cook material, σ_0 can be taken to equal A. Tensile experiments of Hendrickson et al. [39] on prenotched steel plates with a yield stress of 705 MPa deformed at nominal stress rates of $\sim$1–10^4 MPa/s revealed that brittle failure occurred when $\sigma_p/\sigma_0 \simeq 2.34$. This value of σ_p/σ_0 was found to be independent of the temperature and the rate of loading. Here we assume that brittle failure initiates at a point when $\sigma_p/\sigma_0 = 3.0$ there and propagates in the direction of the minimum gradient in σ_p. We add that, to our knowledge, the failure of particulate composites under dynamic loading has not been studied experimentally. However, we have homogenized the material properties and are analyzing the failure of an inhomogeneous body with material properties varying continuously. The local failure criterion appears reasonable since crack tip fields in such a body are similar to those in a homogeneous body. Note that $\sigma_0 = A$ for a thermoviscoplastic material and for a FG body σ_0 is a continuous function of $\mathbf{X}$.

2.7.2. Ductile failure

Ductile failure is generally believed to initiate due to the nucleation and coalescence of voids within an adiabatic shear band (ASB). We recall that the effective plastic strain induced within an ASB exceeds 1. Accordingly, a ductile failure is assumed to ensue at a point when the effective plastic strain equals 1.5 and propagate in the direction of the minimum gradient in the effective plastic strain. Scanning electron micrographs of deformed tungsten heavy alloys reveal that the path of an ASB is unaffected by the presence of stiff W particulates in the relatively soft NiFe matrix [50]. It of course does not imply that the effective plastic strain in W particulates and the NiFe matrix is the same. However, under the premise that a particulate composite can be treated as a homogenized medium the presumed fracture criterion is reasonable.

2.8. Simulation of crack propagation

In order to simulate crack initiation and propagation, we assume that as soon as a failure criterion is met at a node, say N, an additional node N^*, coincident with N but not connected to it, is added to the FE mesh. The node N^* is connected to the node N^{**} that has the next highest value of σ_p for the propagation of the brittle failure and of ε_e^p for the propagation of the ductile failure; note that N^{**} is a preexisting node. The elements are adjusted such that all nodes originally connected to N on one side of the newly formed crack are connected to N^* instead. Thus lines NN^{**} and N^*N^{**} virtually overlap at the instant of the initiation of fracture and each line is the boundary of an element. Note that no new element is created; however, a node is added, the element connectivity is modified and the number of unknowns is increased. Subsequent deformations of the body will either move N and N^* apart thereby creating a gap between them, or tend to push them together which may be accompanied by relative sliding between them. In the former case, surface tractions and the normal component of the heat flux are assumed to be null on the crack surfaces. In the latter case, the contacting surfaces are designated as master and slave, and the distance of a node on the slave

surface from the master surface is determined. If interpenetration occurs, then a Lagrange multiplier-based conjugate gradient method is used to compute the minimum force to be applied to the slave node and the master line segment in order to prevent interpenetration. One returns to the previous time step and applies loads determined by the contact algorithm; this technique is usually called predictor–corrector and has been described by Zywicz and Puso [40], and Carpenter et al. [41]. The algorithm is slow since it requires that the analysis be performed twice for the timestep in which contact occurs. However, the contact detection algorithm is fast, is independent of which master segment a node on the slave surface penetrates, gives normal tractions between contacting surfaces, and permits their relative sliding. Batra and Lear [42] used a penalty method to compute the normal force to be applied to contacting nodes in order to avoid interpenetration.

This technique allows for a crack to propagate along inter-element boundaries. Thus a sufficiently fine FE mesh is needed to get accurate crack path.

3. Computation and discussion of results

3.1. Wave propagation in a linear elastic FG bar

We validate our methodology of analyzing transient deformations of a FG body by studying wave propagation in a linear elastic bar whose Young's modulus, E, mass density ρ, and Poisson's ratio v are given by

$$E = 200(1 + 0.25X_1)\ \text{GPa}, \quad \rho = 10^4(1 + 0.25X_1)^{-1}\ \text{kg/m}^3, \quad v = 0.29. \tag{27}$$

In Eq. (27) X_1 is in mm. Values of material parameters listed in (27) are not for a W/NiFe FGM. These satisfy the condition in Chiu and Erdogan's [44] paper for the existence of an analytical solution. Thus the wave speed $c_w = \left(\frac{E(1-v)}{\rho(1+v)(1-2v)}\right)^{1/2}$ varies affinely from 5.12 km/s at $X_1 = 0$ to 6.40 km/s at $X_1 = 20$ mm. However, the acoustic impedance ($=\sqrt{E\rho}$) is constant throughout the bar. In order to simulate one-dimensional elastic deformations of the bar, all nodes were restrained from moving in the X_2-direction, and the material parameter A was assigned a very high value to suppress plastic deformations. Since the computer code for plane strain deformations tacitly assumes that $u_3 = 0$, therefore, the only non-vanishing component of displacement is u_1. The 20 mm × 0.5 mm bar was divided into 800×20 uniform 4-node quadrilateral elements. Various integrals appearing in the weak formulation of the problem were computed by using the 2×2 quadrature rule with values of material parameters evaluated at the integration points. The same strategy was employed by Batra [43] to analyze static finite plane strain deformations of a body made of an inhomogeneous Mooney–Rivlin material. An analytical solution of the problem, using the Laplace transform technique, has been given by Chiu and Erdogan [44]. It is inverted numerically by employing Laguerre polynomials to find the axial stress and the axial velocity as a function of time t.

Fig. 2a depicts the axial velocity prescribed at the end $X_1 = 0$ of the bar. The time histories of the axial stress at $X_1 = 10$ mm obtained from the numerical and the analytical solutions are compared in Fig. 2b, and the spatial variations of the wave speed obtained from the numerical and the analytical solutions are compared in Fig. 2c. Except for small oscillations, the two sets of results agree with each other. The amplitude of oscillations can be diminished by introducing artificial viscosity but it was not tried.

Various subroutines in the computer code had previously been verified by using the method of ficticious body forces illustrated in Batra and Liang [52]. That is, one assumes a closed form expression for the displacement components and the temperature, finds body forces and sources of internal energy needed to satisfy the balance of linear momentum and the balance of internal energy, and the initial and the boundary conditions. These are input into the computer code. If the computed solution matches with the analytical

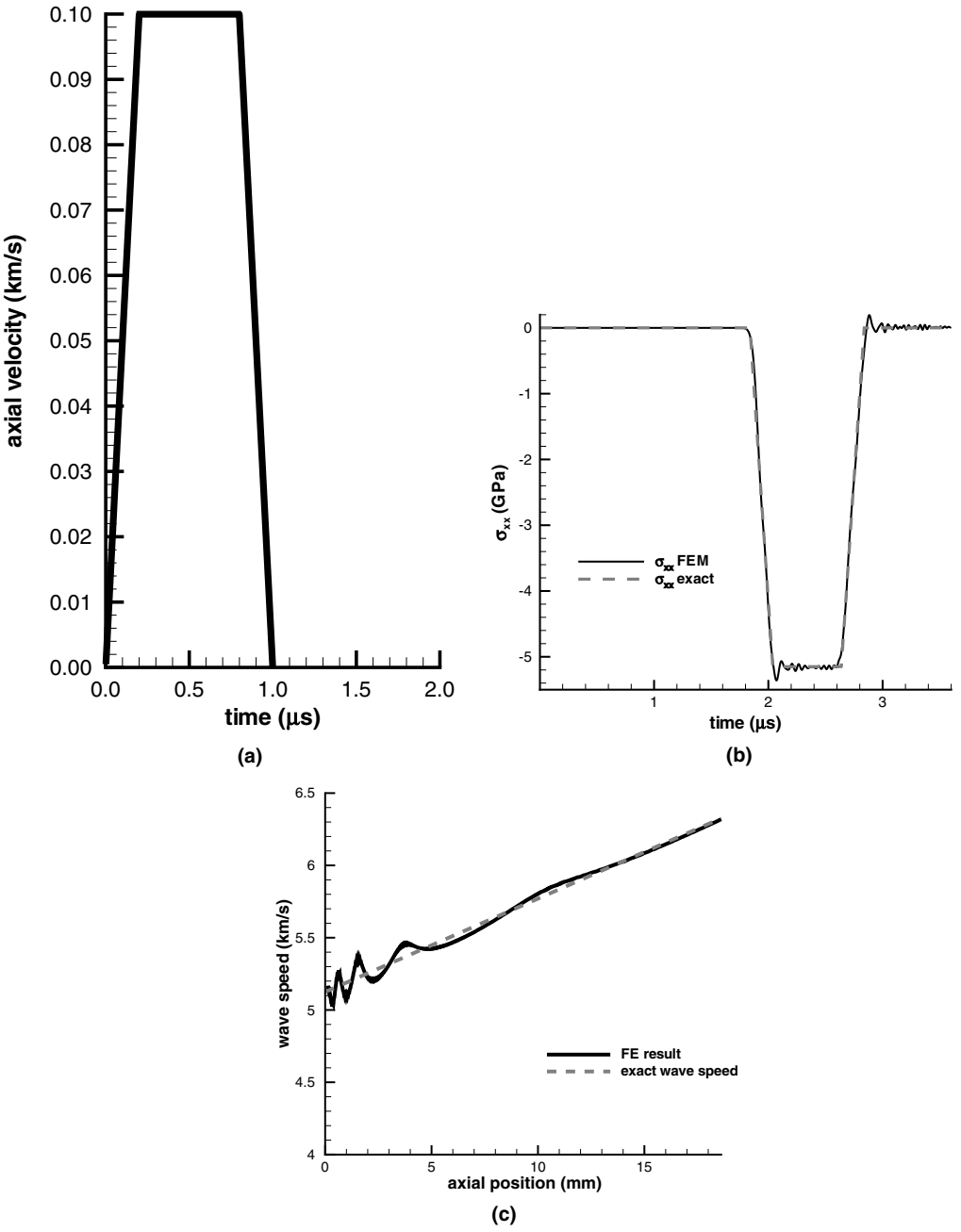

Fig. 2. (a) Time history of the axial velocity prescribed at the left end of the FG bar; (b) comparison of the time histories of the axial stress at $x = 10$ mm obtained from the numerical and the analytical solutions; (c) comparison of the spatial variation of the axial stress at time $t = 15$ μs.

solution of the problem, then the code is verified. Batra and Love [45] have used this code to analyze the initiation and propagation of shear bands in a FG body.

3.2. Simulation of brittle failure

3.2.1. Crack propagation speed

The 10 mm × 10 mm cross-section has an initial sharp crack of length 1 mm at the horizontal centroidal axis with the center of the crack coincident with the centroid of the plate. The plate is deformed at an average axial strain rate of either 200 or 2000 s^{-1}. Values of Young's modulus, E, mass density, ρ, and Poisson's ratio, v, for W and NiFe, and the speeds of the longitudinal wave in a bar and the Rayleigh wave speed are listed in Table 1; values of other material parameters are given in Table 2 and in Eqs. (28). We note that NiFe exhibits considerably higher strain- and strain-rate hardening than W.

Other parameters were assigned the following values for both materials.

$$\begin{aligned} &\dot{\varepsilon}_0 = 1\ s^{-1}, \quad \beta_1 = 1.5, \quad \beta_2 = 1.0, \quad f_2 = 0.04, \quad s_2 = 0.1, \quad \theta_r = 273\ K, \\ &\tau = 10^{-12}\ s, \quad \varepsilon_n = 0.5, \quad f_c = 0.15, \quad f_u = 2/3, \quad f_f = 0.25. \end{aligned} \tag{28}$$

Even though deformations are symmetric about the two centroidal axes, symmetry about the vertical centroidal axis only is exploited to reduce the problem size. The analysis of deformations of the half plate facilitates using the node release technique for studying crack propagation. The FE mesh used to analyze the problem is depicted in Fig. 1a, details of mesh around the crack-tip are given in the inset. The mesh consists of 17,444 4-node isoparametric quadrilateral elements with 1080 elements along the axis of the crack. There are 108 uniform elements behind the crack tip and 972 ahead of it; thus the length of an element is 4.63 μm. The appropriateness of the mesh has been ascertained by ensuring that the computed speed of an elastic wave is very close to the analytic value when E and ρ vary along the direction of propagation of the wave. Once the brittle failure criterion at a node is met, that node is split into two essentially overlapping but unconnected nodes as described in Section 2.7. Thus an elastic unloading wave emanates from the newly created crack surfaces and propagates into the body. The position of the crack-tip at different times is determined and a polynomial is fit to the data. The first derivative of this polynomial fit gives speed, C, of crack propagation as a function of time or the position of the crack-tip. It was found that C so determined is very sensitive to the polynomial fit. Three curve fits with the coefficient of regression >0.999 gave noticeably different values of C. Thus C at a point is taken to equal the slope of the least squares line through 21 points with 10 immediately preceding it and 10 immediately following it. The Rayleigh wave speed and the crack propagation speed, C, versus the crack length for nominal strain rates of 200 and 2000 s^{-1} are depicted in Fig. 3a–d. Freund's [46] analysis of crack propagation in an infinite homogeneous elastic body shows that the maximum crack propagation speed equals the Rayleigh wave speed; Eischen [7]

Table 1
Material parameters and wave speeds for NiFe and W

Material	Young's modulus (GPa)	Poisson's ratio	Mass density (kg/m^3)	Bar wave speed (m/s)	Acoustic impedance $(E\rho)^{0.5}$ ($kg/m^2 s$)	Rayleigh wave speed (m/s)
NiFe	255	0.29	9200	5265	48.44×10^6	3035
W	400	0.29	19,300	4552	87.86×10^6	2624

Table 2
Values of material parameters for NiFe and W

Material	A (MPa)	B (MPa)	$\widetilde{C}$	θ_m (K)	c (J/kg K)	κ (W/(m K))	$\hat{\alpha}$ ($10^{-6}\ K^{-1}$)	m	n
NiFe	150.0	546.0	0.0838	1225	382	100	15	1.0	0.208
W	730.0	562.0	0.029	1723	138	160	5.3	1.0	0.0751

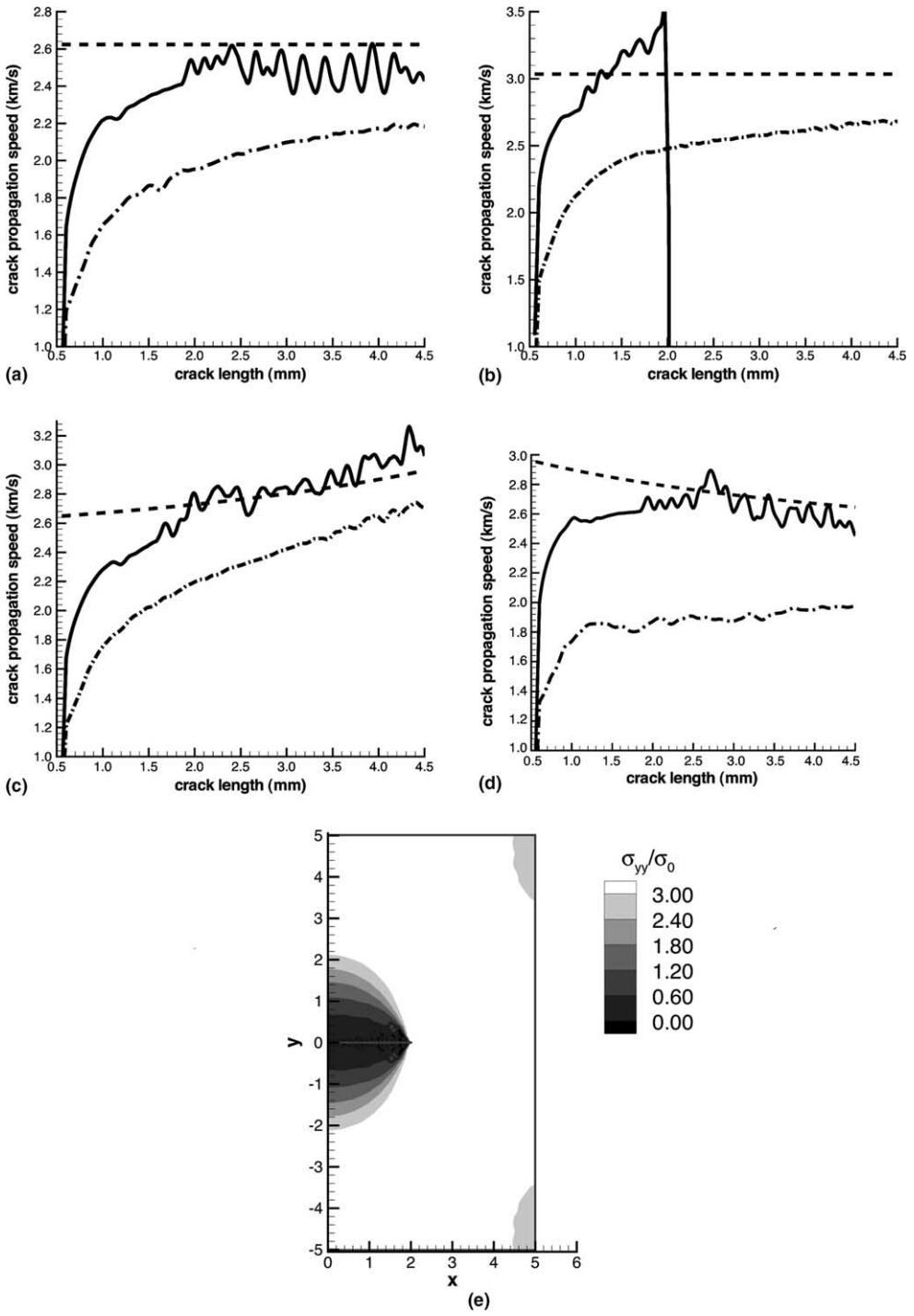

Fig. 3. Crack propagation speed versus crack length at nominal strain rates of 200 and 2000 s^{-1} in a (a) tungsten, (b) nickel–iron, (c) W2NiFe, and (d) NiFe2W plate; (- - - Rayleigh wave speed; — crack speed at nominal strain-rate = 200 s^{-1}; – · – crack speed at nominal strain-rate = 2000 s^{-1}). (e) Shattered region in the NiFe plate deformed at a nominal strain rate of 2000 s^{-1} is unshaded.

has proved a similar result for inhomogeneous materials. For each one of the two homogeneous and the two FG plates, C for the nominal strain rate of 2000 s^{-1} is higher than that for the nominal strain rate of 200 s^{-1}. For the W plate deformed at 200 s^{-1}, C increases as the crack propagates to the right edge of the plate but at the higher strain rate of 2000 s^{-1}, it soon approaches a steady value that is a little less than the Rayleigh wave speed. For a NiFe plate deformed at 2000 s^{-1}, the crack propagates to the right for a little while and then a large region of the plate ahead of the crack fails instantaneously as indicated by the maximum principal tensile stress exceeding $3\sigma_0$ simultaneously everywhere in this region. It is signified in Fig. 3b by the sudden drop in the crack propagation speed C; the shattered region is depicted in Fig. 3e as unshaded.

For the W2NiFe FG plate, C continues to increase with the crack extension, is always less than the Rayleigh wave speed when the plate is deformed at 200 s^{-1} but approaches the Rayleigh wave speed when the nominal strain rate is 2000 s^{-1}. Except for differences in magnitudes, the curves in Fig. 2a and c are similar. Thus as far as crack propagation due to brittle failure is concerned, the W and the W2NiFe plates behave alike. However, for the NiFe2W FG plate, even though the Rayleigh wave speed decreases monotonically with the distance from the left edge because of the spatial variation in the material properties, the computed crack speed C first increases and approaches essentially a steady value after the crack has propagated a certain distance. The crack speed is higher when the nominal strain rate equals 2000 s^{-1} than that when the nominal strain rate is 200 s^{-1}. No shattering of the NiFe2W plate at either one of the two nominal strain-rates is observed.

3.2.2. Shattering phenomenon

Returning to the shattering of the NiFe plate, several numerical experiments were conducted by varying the nominal axial strain rate. It was found that at a nominal axial strain rate of 3000 s^{-1} the plate shattered as soon as the crack began to advance. The plate shattered at nominal axial strain rates exceeding 1130 s^{-1} but did not shatter at a nominal axial strain rate of 1120 s^{-1}. The crack extension/elongation at the instant of the plate shattering decreased with an increase in the nominal axial strain rate; it equaled $\sim$2.01, 1.47 and 0.741 mm for nominal axial strain rates of 1130, 2000 and 3000 s^{-1} respectively.

3.2.3. Axial force

We have plotted in Fig. 4 the variation of the computed axial load as the crack propagates to the right. Small oscillations in the load due to the arrival of unloading waves emanating from the newly formed crack surfaces have been diminished by using the smoothing option in TecPlot. At a strain rate of 200 s^{-1}, the crack propagation is stable in both pure W and W2NiFe FG plates as signified by either the load remaining essentially steady or increasing except when the crack has propagated to a point near the right edge. At the higher strain rate of 2000 s^{-1}, the axial load for pure W plate remains nearly constant at $\sim$4.67 kN till the crack-tip has advanced by 1.75 mm and then slowly increases except when the crack tip is close to the outer edge of the plate. When the precracked W plate is pulled at a nominal axial strain rate of 200 s^{-1}, the axial load continues to increase slowly till the crack length equals 2.2 mm and then gradually decreases. Recall that the surface area of the horizontal plane containing the crack decreases as the crack extends, and except for the first 1 μs, the bar is being pulled with a uniform axial velocity. Thus the working of external forces is proportional to the axial force. The variation of the axial load with the advance of the crack in NiFe and NiFe2W FG plates is similar to that in the W plate except that a large chunk of material ahead of the crack suddenly fails in the pure NiFe plate deformed at a nominal strain rate of 2000 s^{-1}. For the NiFe2W plate, the variation of the axial load with the crack length is similar to that for the W2NiFe plate.

3.2.4. J-integral

A detailed examination of stresses and strains induced within the specimen revealed that deformations were virtually elastic everywhere except near the crack-tip where small plastic strains developed; the size of

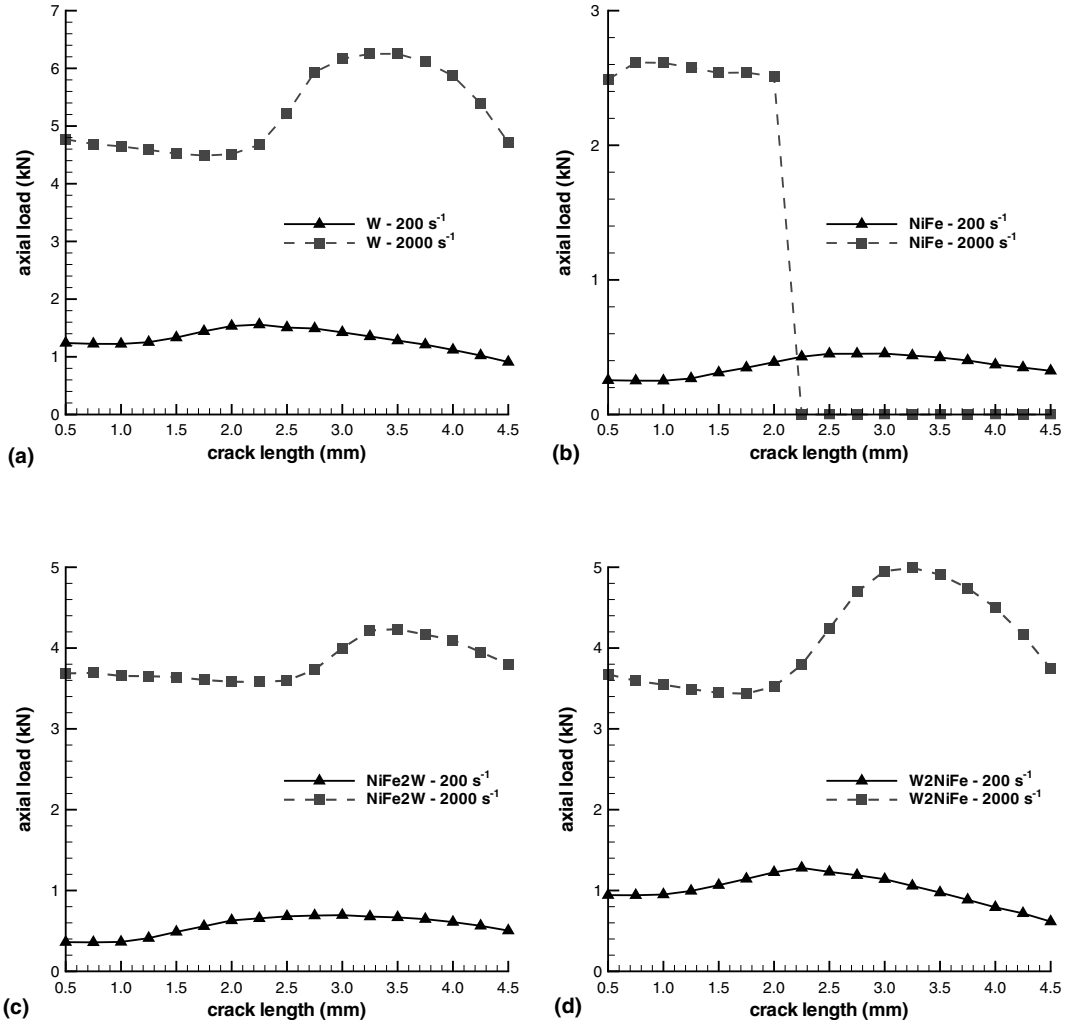

Fig. 4. Axial load versus crack length at axial nominal strain rates of 200 and 2000 s^{-1} for a precracked (a) tungsten, (b) nickel–iron, (c) W2NiFe, and (d) NiFe2W plate.

this "process zone" is negligible as compared to the crack length. In order to see if concepts of the strain energy release rate or the J-integral can be used, we computed the J-integral defined by

$$J = \lim_{\Gamma \to 0} \int_{\Gamma} \left[(w + T)\,\mathrm{d}x_2 - \sigma_{ij} n_j \frac{\partial u_i}{\partial x_1}\,\mathrm{d}s \right],$$
$$w = \int_0^t \sigma_{ij} D_{ij}\,\mathrm{d}t, \quad T = \frac{1}{2}\rho v_i v_i, \quad u_i = x_i - X_\alpha \delta_{i\alpha}. \tag{29}$$

Here Γ is a closed contour enclosing the crack tip, and ds is an element of arc length on Γ. Fig. 5a exhibits the value of the J-integral as a function of the crack tip location for the pure W specimen deformed at nominal strain rates of 200 and 2000 s^{-1}. The contour Γ used to evaluate the J-integral appeared stationary to an observer always situated at the crack tip and hence moving with it. The contour Γ spanned 5 elements behind the crack tip, 5 elements ahead of it and 10 elements perpendicular to the crack-axis, each element is

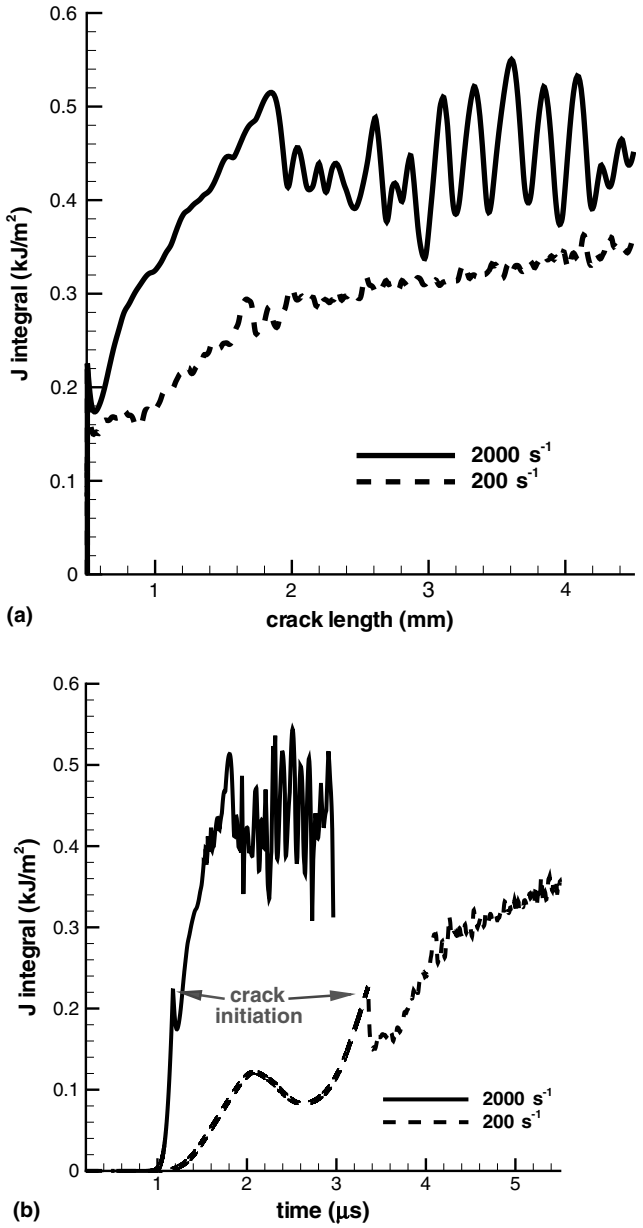

Fig. 5. In a W plate variation of the J-integral with (a) the crack extension and (b) time.

of length 4.63 μm, and the length of the starter half-crack is 500 μm. For an average axial strain-rate of 200 s^{-1}, the J-integral increases monotonically signifying an increasing resistance to crack propagation. However, at the average axial strain-rate of 2000 s^{-1}, the J-integral first increases with an advance in the crack tip but then oscillates wildly. These oscillations cannot be attributed to the contour Γ used to evaluate J since a similar contour with respect to the crack tip gave reasonable values of the J-integral for all locations of the crack tip at the lower strain rate of 200 s^{-1} and for earlier stages of the crack propagation in the

plate deformed at an axial strain rate of 2000 s^{-1}. The time history of the evolution of the J-integral is exhibited in Fig. 5b where its values at the instants of crack initiation are also shown. Values of the J-integral at the instant of crack initiation in the W-plate are the same and equal $\sim$0.22 kJ/m^2 at axial nominal strain rates of 200 and 2000 s^{-1}.

3.3. Simulation of ductile failure

In order to simulate crack propagation due to ductile failure we analyze plane strain thermomechanical deformations of a block of material with equal and opposite tangential velocities prescribed on its top and bottom surfaces as described in Section 2. Thus the steady-state nominal strain-rate is v_0/H, and equals 5000 s^{-1} for simulations discussed herein. The FE mesh used to analyze the problem is depicted in Fig. 1b. The elements are of size 4.6 μm × 4.6 μm in the central and end portions but are larger in other regions. For the FG bodies, the composition varies from either 0% W at the centroid to 100% W at the edges or vice-a-versa. The yield stress of the material of elements in the 4.6 μm thick 0.2 mm long layers located symmetrically about the centroidal axis was reduced by 30% so as to nucleate an adiabatic shear band (ASB) there. Recall that a crack is assumed to open at a point when the effective plastic strain there equals 1.5. It was found that the ASB and the crack propagate horizontally with equal and opposite velocities; thus their propagation to the right is described below.

3.3.1. Crack speed

Figs. 6 and 7 depict the variation in the crack length, the ASB length, the crack tip speed and the ASB speed as they advance in the two homogeneous materials, namely W and NiFe, and the FGM W2NiFe. For the NiFe2W FG plate, in spite of the rather strong defect at the centroid, the crack originated from points $(-L, 0)$ and $(L, 0)$ and propagated inwards. Thus it propagated from W rich region to NiFe rich region, and the situation is similar to that for crack propagation in the W2NiFe FG plate. An ASB initiates at a point when the effective plastic strain there equals 1.5; thus the difference between an ASB and a crack is that new thermally insulated traction free surfaces are created when a crack opens but the material is intact during the initiation and propagation of an ASB. Because of the compressive normal stress acting on the crack surfaces, they always contact each other. In W, the time histories of the crack length and the ASB length and hence their speeds of propagation are virtually identical. However, in NiFe the crack length is larger than the ASB length. Hence the crack propagation speed is higher than the ASB speed. Except when the ASB/crack arrives at $x_1 = \pm L$, its speed increases from $\sim$0.1 km/s at origination to $\sim$1.8 km/s at the end. The crack accelerates slowly in the beginning but quite rapidly towards the end. Note that an ASB/crack initiates in NiFe at 165 μs but in W at 35 μs. Interestingly, the time histories of the crack propagation speeds in W and NiFe are nearly coincident. Whether it is so in all homogeneous materials remains to be seen. Had we assumed that an ASB forms at the effective plastic strain of 1.0 and a crack opens at the effective plastic strain of 1.5, the ASB length would have been larger than the crack length. However, their speeds of propagation would be essentially the same.

Batra and Zhang [51] analyzed three-dimensional deformations of a thin-wall steel tube by using the computer code DYNA3D. A weak element was introduced to trigger the initiation of an ASB and the tube was deformed by applying equal and opposite tangential velocities to the end faces. Contours of the effective plastic strain of 1.0 or higher were found to propagate at nearly the same speed. It was found that the ASB speed depended upon the nominal strain rate, and it gradually increased as the ASB propagated circumferentially outwards from the point of initiation. These results agree qualitatively with those reported herein. Batra and Lear [27] used an in-house developed code based on the same equations as those in this paper and 3-node triangular elements. They found that in plane strain tensile deformations of a W plate the ASB speed varied from 165 m/s at the instant of initiation to 357 m/s after it had traversed $\sim$3 mm. It differs from that found here partly because in plane strain shear deformations an ASB propagates in the direction

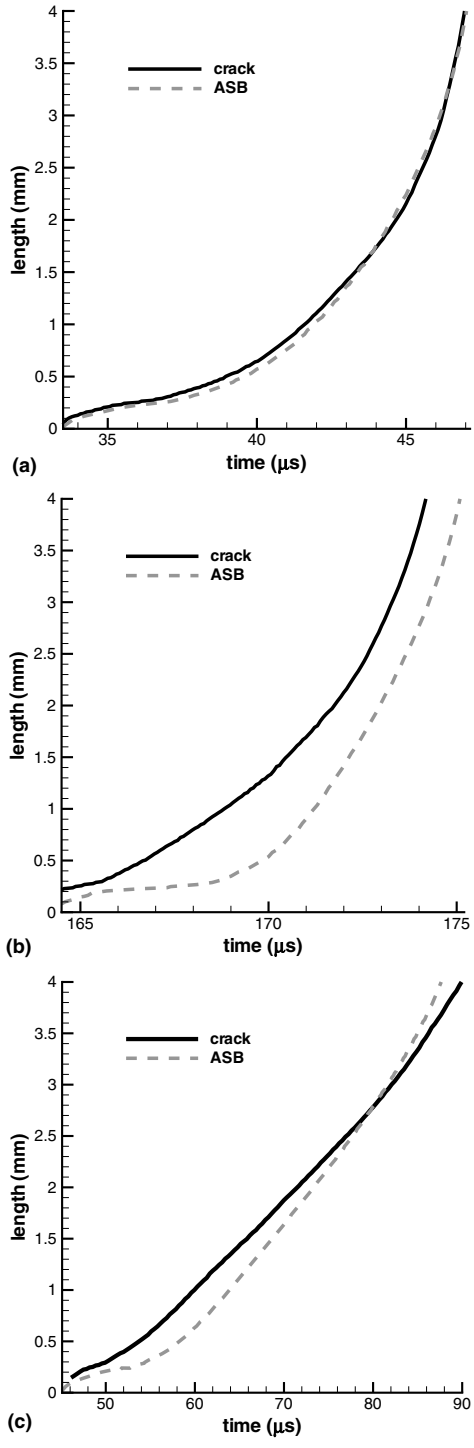

Fig. 6. Time histories of the evolution of the ASB and the crack in (a) W, (b) NiFe and (c) W2NiFe plates deformed in plane strain shear.

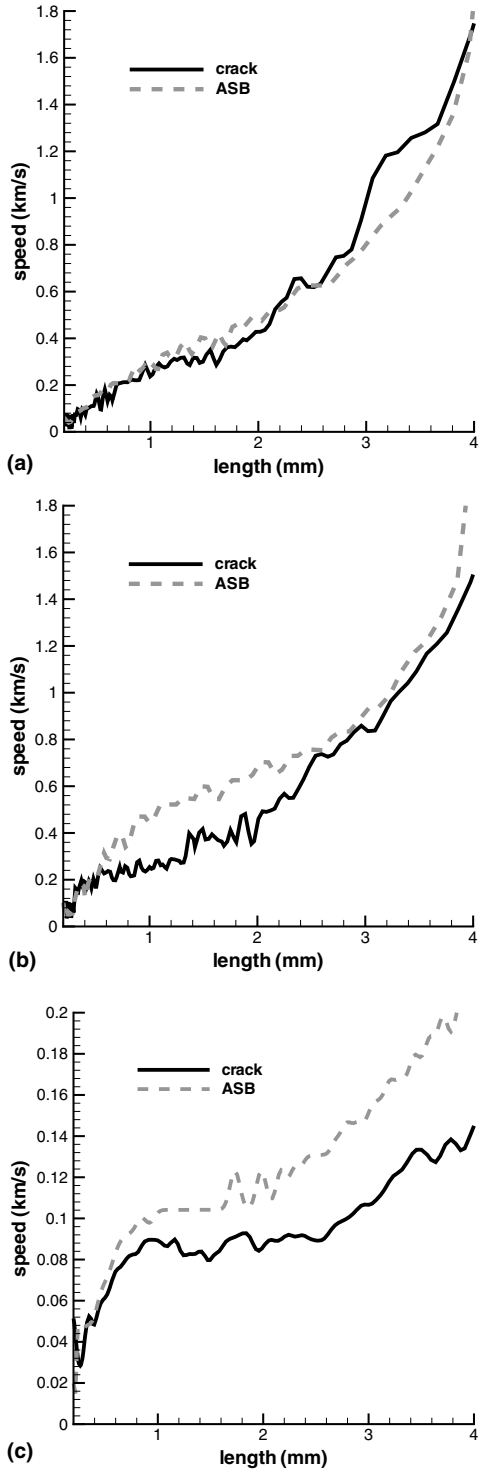

Fig. 7. Variation of the crack and the ASB speeds in (a) W, (b) NiFe and (c) W2NiFe plates deformed in plane strain shear.

of the applied velocity but in plane strain tensile deformations the ASB propagation direction makes an angle of ~45° to the loading direction.

In W2NiFe FGM plate, the ASB/crack initiation time is between those for the pure W and the pure NiFe plates; a similar situation occurs in the brittle failure of these materials. The ASB/crack propagation speed in the FGM plate is significantly less (approximately by an order of magnitude) than that in either one of its two constituents.

For ductile fracture, there are significant plastic deformations induced, so the J-integral is not evaluated.

3.3.2. Applied tangential force

We have plotted in Fig. 8 time-histories of the tangential force required to deform the specimen. Since the top and the bottom surfaces are constrained from moving in the vertical direction, the working of external forces is due to tangential tractions. Furthermore, this working is proportional to the tangential surface traction as the tangential velocity, except for the first 1 μs, is constant. As expected the tangential force decreases with the opening of a crack and it continues to decrease as the crack elongates. With the crack extension, smaller surface area supports the external load. Also, with continued plastic deformations, the material softens and its capacity to support external load diminishes. The rate of decrease of the applied tangential force is higher for W than that for NiFe since the strain and strain-rate hardening effects are higher in NiFe than in W. With the extension of the crack, the driving force drops more rapidly for the FGM plate than that for the two homogeneous plates.

3.4. Effect of crack opening on deformation fields

In order to delineate the differences, if any, between the deformation fields ahead of the ASB tip and the crack tip, we have plotted in Fig. 9 the spatial variation of the effective plastic strain rate in a W plate deformed at a nominal strain rate of 200 s^{-1}. Because of the unloading elastic waves emanating from newly formed crack surfaces, the strain rates ahead of the crack-tip are oscillatory; cf. Fig. 9a. The effective plastic strain rate at the crack tip is finite. However, it varies rapidly at points with $10^{-2.3} \leqslant r/a \leqslant 10^{-1}$ where r is the distance of a point from the crack tip and a equals the crack length. The slope of the line obtained by least squares fit to the computed values equals approximately -0.4. Results plotted in Fig. 9b indicate that, once an ASB has developed, then the spatial variation of the effective plastic strain-rate ahead of the ASB tip varies very slowly and its value at the ASB tip equals $\sim 1.31 \times 10^5$ s^{-1}. It does not exhibit the singularity prevalent in the effective plastic strain-rate ahead of the crack tip.

We have plotted in Fig. 10a–c the distribution of the temperature rise in W, NiFe and W2NiFe plates at $t = 40$, 170 and 70 μs respectively. These times correspond to instants when the ASB/crack has propagated ~1 mm from the point of initiation. Temperatures at the ASB/crack tips at these times are listed in Table 3.

Thus the temperature rise at the crack tip is nearly 14 K higher than that at the ASB tip. For the case of no crack opening, the maximum temperature occurs at the specimen centroid and not at the ASB tip. This is because, with the passage of time, the difference between the effective plastic strain at the specimen centroid from where an ASB first originated and that at the ASB tip continues to increase; e.g. see Fig. 9b. However, when a crack is formed, then the maximum temperature occurs at the crack tip. Values listed in Table 3 depend upon the ASB/crack initiation criterion.

3.4.1. Relative sliding between surfaces

The relative sliding between the upper and the lower parts of the body is exhibited in Fig. 11 that shows the deformed shape of a small region. It is clear that the part of the body occupying the region $X_2 > 0$ in the reference configuration has moved to the right relative to that in the domain $X_1 < 0$. For example points A and B shown in Fig. 11 coincided with each other in the reference configuration. Recalling that the FE mesh in the reference configuration has rectangular elements with sides parallel to the horizontal and the vertical

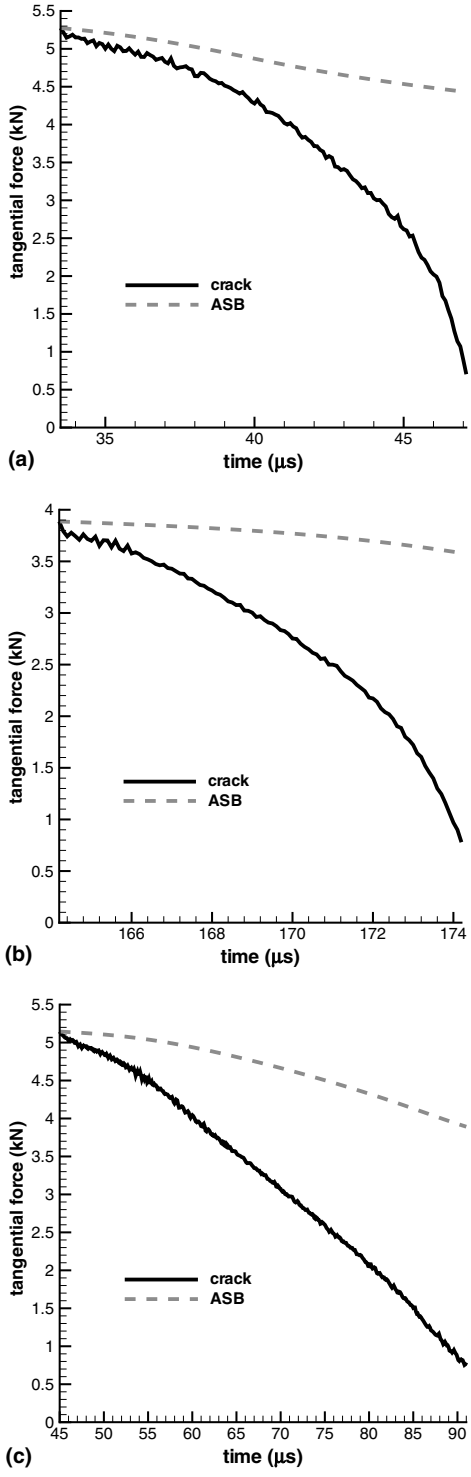

Fig. 8. Time histories of the applied tangential force in (a) W, (b) NiFe and (c) W2NiFe plates deformed in plane strain shear.

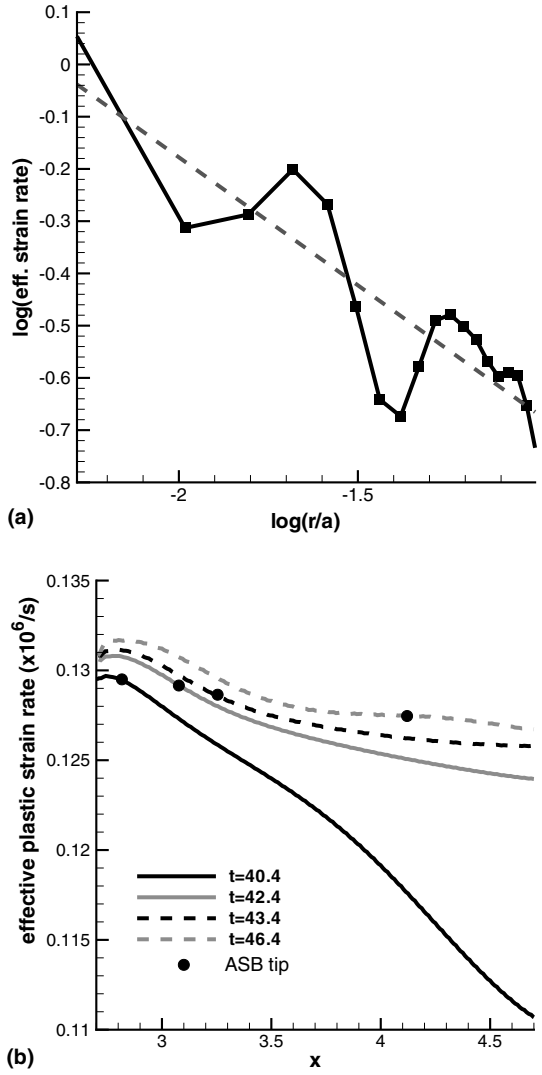

Fig. 9. In (a) W plate, variation of the effective plastic strain-rate ahead of the crack tip, and (b) along the ASB at different times.

axes, the two elements in the vertical direction next to the sliding/crack surface have been sheared considerably more than those further away from the crack surface. The slight asymmetry in the results about the horizontal centroidal axis is attributed to numerical oscillations in the computed results. The smoothing of oscillations located the crack surface at $X_2 = 0.001$ rather than at $X_2 = 0.0$.

3.4.2. Porosity evolution

The hydrostatic pressure in the material within the ASB, ahead of it and directly in front of the crack tip was found to be compressive. Thus no new voids nucleated in the material even though it had enormous plastic deformations. The total porosity evolved in the intensely deformed region is rather minuscule.

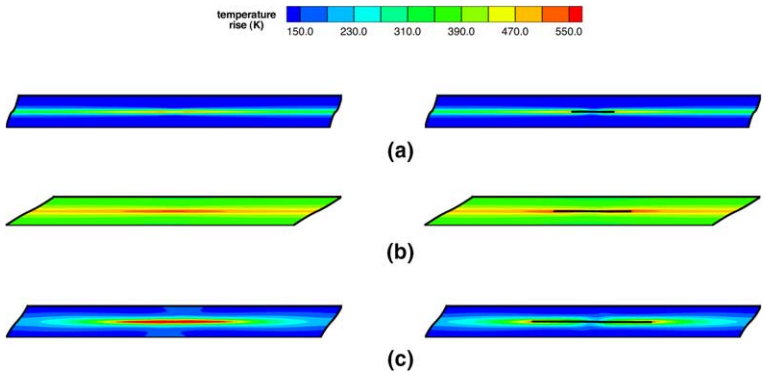

Fig. 10. Temperature distribution in (a) W, (b) NiFe and (c) W2NiFe FGM plates at $t = 40$, 170 and 70 μs respectively. Plots on the left (right) are without (with) crack opening.

Table 3
Temperature rise at ASB/crack tip

Material	ASB tip (K)	Crack tip (K)
W	512	526
NiFe	547	561
W2NiFe	546	561

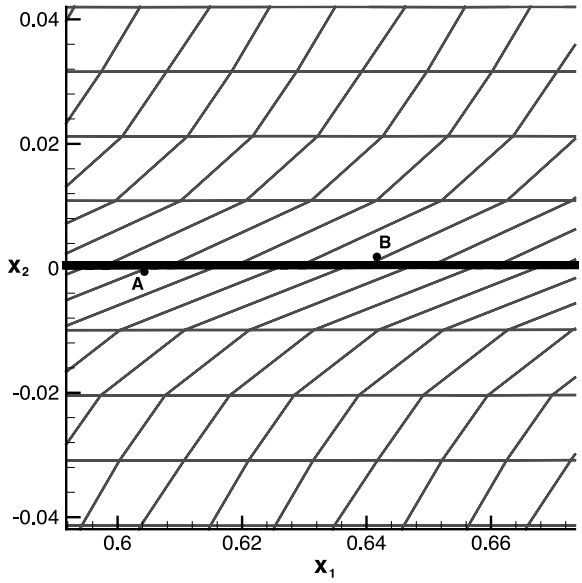

Fig. 11. A section of the W plate deformed in plane strain shear showing relative sliding between the cracked surfaces; point A initially coincided with point B.

3.5. Dependence of results upon the FE mesh

In Section 3.1 we showed that an element size of 25 μm × 25 μm for a FG linear elastic bar gives numerical results close to the analytical solution of the wave propagation problem. In a previous study [45] on

adiabatic shear banding in plane strain tensile deformations of a thermoviscoplastic body, numerical experiments with uniform FE meshes of element size 42 μm × 42 μm and 125 μm × 125 μm gave ASB initiation times differing by 2.1%. These tests suggest that FE meshes used herein should give reasonably accurate results. The CPU time needed to compute speeds of propagation of an ASB and a crack due to ductile failure in a FG body is close to 200 h. Thus, results could not be computed with a FE mesh much finer than the one used here, and for several loading rates.

One way to eliminate the effect of the FE mesh on computed results is to use a strain-rate gradient dependent viscoplasticity theory such as that employed in [47–49]. It introduces material characteristic lengths that cannot be easily estimated.

3.6. Remarks

For all problems studied herein the porosity evolution is negligible. In the plane strain tensile deformations of a precracked plate, the effective plastic strains induced are miniscule and thus way below the threshold value for the nucleation of new voids. In the plane strain shear deformations, the hydrostatic pressure is compressive and again no new voids nucleate. Thus for all practical purposes, results have been computed by using the von Mises yield surface with the flow stress depending upon the effective plastic strain, the effective plastic strain rate and the temperature. These hardening and softening effects play a negligible role during the analysis of brittle failure but are dominant in the analysis of ASBs and the resulting ductile failure.

Because of the homogenization of material properties we have glossed over sharp gradients in deformation likely to occur near interfaces between the matrix and the particulates; e.g. see [54]. Furthermore, extensive plastic deformations during the ductile failure may debond particulates from the matrix. It is possible that effective material properties also depend upon the sizes, shapes and distributions of particulates even though Young's modulus and Poisson's ratio computed from the Mori–Tanaka [35] scheme agree reasonably well with the experimental values. In the absence of test data on the fracture of heterogeneous solids comprised of thermoelastoviscoplastic constituents, the validity of the presently computed results cannot be ascertained.

4. Conclusions

We have analyzed the initiation and propagation of brittle and ductile fractures in homogeneous and functionally graded plates deformed either in plane strain tension at nominal strain rates of 200 and 2000 s^{-1} or in plane strain shear at a nominal strain rate of 5000 s^{-1}. It is found that for the crack propagating due to brittle failure at the axial nominal strain rate of 200 s^{-1}, the axial force is a non-decreasing function of the crack extension. At the higher strain rate of 2000 s^{-1} the axial force increases as the crack extends till the crack length equals approximately one-half the plate width, and it subsequently decreases. When the crack length in a NiFe plate deformed at an average axial strain-rate of 2000 s^{-1} equals about one-half the plate width, a large region of the material ahead of the crack tip fails instantaneously signifying shattering of the plate. It is found that the NiFe plate shatters only if the nominal axial strain rate exceeds 1130 s^{-1}, and the crack elongation prior to shattering varies with the nominal axial strain rate. For the finite size plate studied here, the maximum computed crack speed in a FG plate pulled at a nominal axial strain rate of 2000 s^{-1} is almost equal to the Rayleigh wave speed. For a FG plate, the Rayleigh wave speed varies with the position.

We have also analyzed ductile failure in a plate deformed in plane strain simple shear. It is found that in a W plate, an adiabatic shear band (ASB) and a crack propagate at virtually identical speeds. However, in a NiFe plate the crack speed is higher than the ASB speed in the beginning but the two are nearly equal after

they have propagated for 15 μs. In W and NiFe plates, the crack speed increases from ~0.05 km/s at the instant of initiation to ~1.8 km/s when the crack tip has approached the edge of the plate. However, in a FG plate with the crack propagating from W rich to W poor regions, the crack propagation speed is nearly steady for a certain interval, and its maximum value is about 1/10th of that in a homogeneous W or NiFe plate. The tangential force applied at the top and the bottom surfaces decreases as the ASB/crack extends, and is lower when a crack is allowed to open than that without the opening of a crack. The effective plastic strain-rate is finite at the crack tip but is singular at points slightly ahead of the propagating crack-tip; the order of singularity is ~0.4. However, the effective plastic strain-rate ahead of a propagating ASB varies rather gradually and equals $\sim 1.3 \times 10^5\ s^{-1}$ in a W plate deformed at a nominal strain-rate of $5000\ s^{-1}$. The temperature at a crack tip is ~14 K higher than that at an ASB tip, and equals 526 K and 561 K in W and NiFe plates respectively.

Acknowledgement

This work was partially supported by the NSF grant CMS0002849, the ONR grants N00014-98-1-0300 and N00014-03-MP-2-0131, the ARO grant DAAD19-01-1-0657 and the AFOSR MURI to Georgia Institute of Technology with a subcontract to Virginia Polytechnic Institute and State University. Views expressed in the paper are those of authors and not of funding agencies.

References

[1] Wang Z, Nakamura T. Simulations of crack propagation in elastic–plastic graded materials. Mech Mater 2004;36:601–22.
[2] Hasselman DPH, Youngblood GE. Enhanced thermal stress resistance of structural ceramics with thermal conductivity gradient. J Am Ceram Soc 1978;61:49–52.
[3] Qian LF, Batra RC. Design of bidirectional functionally graded plate for optimal natural frequencies. J Sound Vib 2005;280:415–24.
[4] Batra RC, Jin J. Natural frequencies of a functionally graded rectangular plate. J Sound Vib [available online].
[5] Erdogan F. Fracture mechanics of functionally graded materials. Compos Engng 1995;5:753–70.
[6] Jin ZH, Noda N. Crack-tip singular fields in nonhomogeneous materials. ASME J Appl Mech 1994;61:738–40.
[7] Eischen JW. Fracture of nonhomogeneous materials. Int J Fract 1987;34:3–22.
[8] Honein T, Herrmann G. Conservation laws in nonhomogeneous plane elastostatics. J Mech Phys Solids 1997;45:789–805.
[9] Gu P, Asaro RJ. Crack deflection in functionally graded materials. Int J Solids Struct 1997;34:3085–98.
[10] Becker Jr TL, Cannon RM, Ritchie RO. Finite crack kinking and *T*-stresses in functionally graded materials. Int J Solids Struct 2001;38:5545–63.
[11] Jin ZH, Batra RC. Some basic fracture mechanics concepts in functionally graded materials. J Mech Phys Solids 1996;44:1221–35.
[12] Jin Z-H, Batra RC. *R*-Curve and strength behavior of a functionally graded material. Mater Sci Engng A 1998;242:70–6.
[13] Atkinson C, List RD. Steady state crack propagation into media with spatially varying elastic properties. Int J Engng Sci 1978;16:717–30.
[14] Ma L, Wu L-Z, Zhou Z-G, Zeng T. Crack propagating in a functionally graded strip under the plane loading. Int J Fract 2004;126:39–55.
[15] Lee KH. Characteristics of a crack propagating along the gradient in functionally gradient materials. Int J Solids Struct 2004;41:2879–98.
[16] Tvergaard V. Theoretical investigation of the effect of plasticity on crack growth along a functionally graded region between dissimilar elastic–plastic solids. Engng Fract Mech 2002;69:1635–45.
[17] Jin ZH, Dodds RH. Crack growth resistance behavior of a functionally graded material: computational studies. Engng Fract Mech 2004;71:1651–72.
[18] Gurson AL. Continuum theory of ductile rupture by void nucleation and growth: Part I. J Engr Mater Tech 1977;99:2–15.
[19] Tvergaard V. Influence of voids on shear band instabilities under plane strain conditions. Int J Fract 1981;17:389–407.
[20] Johnson GR, Cook WH. A constitutive model and data for metals subjected to large strains, high strain-rates, and high temperatures. In Proc 7th Int Symp on Ballistics, 1983. p. 541–7.
[21] Chu C, Needleman A. Void nucleation effects in biaxially stretched sheets. J Engng Mater Tech 1980;102:249–56.

[22] Tvergaard V, Needleman A. Analysis of the cup–cone fracture in a round tensile bar. Acta Metall 1984;32:157–69.
[23] Budiansky B. Thermal and thermoelastic properties of isotropic composites. J Compos Mater 1990;4:701–44.
[24] Jiang B, Batra RC. Effective properties of a piezocomposite containing shape memory alloy and inert inclusions. Continuum Mech Thermodyn 2002;14:87–111.
[25] Cattaneo C. A form of heat equation which eliminates the paradox of instantaneous propagation. CR Acad Sci 1958;247:431–3.
[26] Vernotte P. The true heat equation. CR Acad Sci 1958;247:2103.
[27] Batra RC, Lear MH. Adiabatic shear banding in plane strain tensile deformations of eleven thermoelastoviscoplastic materials with finite thermal wave speed. Int J Plast [in press].
[28] Batra RC, Chen L. Effect of viscoplastic relations on the instability strain, shear band initiation strain, the strain corresponding to the minimum shear band spacing, and the band width in a thermoviscoplastic material. Int J Plast 2001;17:1465–89.
[29] Batra RC. On heat conduction and wave propagation in non-simple rigid solids. Lett Appl Engng Sci 1975;3:97–107.
[30] Batra RC, Kim KH. Effect of viscoplastic flow rules on the initiation and growth of shear bands at high strain rates. J Mech Phys Solids 1990;38:859–74.
[31] Batra RC, Jaber NA. Failure mode transition speeds in an impact loaded prenotched plate with four thermoviscoplastic relations. Int J Fract 2001;110:47–71.
[32] Batra RC, Chen L. Shear band spacing in gradient-dependent thermoviscoplastic materials. Comput Mech 1999;23:8–19.
[33] Batra RC. Steady state penetration of thermoviscoplastic targets. Comput Mech 1988;3:1–12.
[34] Bodner SR, Partom Y. Constitutive equations for elastic–viscoplastic strain-hardening materials. J Appl Mech 1975;56:385–9.
[35] Mori T, Tanaka K. Average stress in matrix and average elastic energy of materials with misfitting inclusions. Acta Metall 1973;21:571–4.
[36] Suquet P. Overall potentials and extremal surfaces of power law or ideally plastic composites. J Mech Phys Solids 1993;41.
[37] Hughes TJR. The finite element method. New Jersey: Prentice Hall; 1987.
[38] Ritchie RO, Knott JF, Rice JR. On the relationship between critical tensile stress and fracture toughness in mild steel. J Mech Phys Solids 1973;21:395–410.
[39] Hendrickson JA, Wood DS, Clark DC. The initiation of brittle fracture in mild steel. J Mech Phys Solids 1958;50:656–81.
[40] Zywicz E, Puso M. A general conjugate-gradient-based predictor–corrector solver for explicit finite element contact. Int J Numer Meth Engng 1999;44:439–59.
[41] Carpenter N, Taylor R, Katona M. Lagrange constraints for transient finite element surface contact. Int J Numer Meth Engng 1991;32:103–28.
[42] Batra RC, Lear MH. Simulation of brittle and ductile fracture in an impact loaded prenotched plate. Int J Fract 2004;126: 179–203.
[43] Batra RC. Finite plane strain deformations of rubberlike materials. Int J Numer Meth Engng 1980;15:145–60.
[44] Chiu TC, Erdogan F. One-dimensional wave propagation in a functionally graded medium. J Sound Vib 1999;222:453–87.
[45] Batra RC, Love BM. Adiabatic shear bands in functionally graded materials. J Therm Stresses [in press].
[46] Freund LB. Crack propagation in an elastic solid subjected to general loading—III. Stress wave loading. J Mech Phys Solids 1973;21:47–61.
[47] Batra RC. The initiation and growth of, and the interaction among adiabatic shear bands in simple and dipolar materials. Int J Plast 1987;3:75–89.
[48] Batra RC, Kim CH. Adiabatic shear banding in elastic–viscoplastic nonpolar and dipolar materials. Int J Plast 1990;6:127–41.
[49] Batra RC, Hwang J. Dynamic shear band development in dipolar thermoviscoplastic materials. Comput Mech 1994;12:354–69.
[50] Dick RD, Ramachandran V, Williams JD, Armstrong RW, Holt WH, Mack W. Dynamic deformation of W7Ni3Fe alloy via reverse-ballistic impact. In: Crowson A, Chen ES, editors. Tungsten and tungsten alloys—recent advances. The Minerals, Metals & Materials Society; 1991. p. 269–76.
[51] Batra RC, Zhang X. On the propagation of a shear band in a steel tube. J Engng Mater Technol 1994;116:155–61.
[52] Batra RC, Liang XQ. Finite dynamic deformations of smart structures. Comput Mech 1997;20:427–38.
[53] Love BM, Batra RC. Determination of effective thermomechanical parameters of a mixture of two elastothermoviscoplastic constituents, submitted for publication.
[54] Batra RC, Love BM. Mesoscale analysis of shear bands in high strain rate deformations of tungsten/nickel–iron composites. J Therm Stresses [in press].